The Astrophysical Journal, 990:94 (8pp), 2025 September 10 https://doi.org/10.3847/1538-4357/adf55c

The X-Ray Link between High Eddington Ratio Dust-obscured Galaxies (DOGs) and Hot DOGs

Fan Zou[1], W. N. Brandt[2,3,4], Elena Gallo[1], Fabio Vito[5], and Zhibo Yu[2,3]
[1] Department of Astronomy, University of Michigan, 1085 S University Avenue, Ann Arbor, MI 48109, USA; fanzou01@gmail.com
[2] Department of Astronomy and Astrophysics, 525 Davey Laboratory, The Pennsylvania State University, University Park, PA 16802, USA
[3] Institute for Gravitation and the Cosmos, The Pennsylvania State University, University Park, PA 16802, USA
[4] Department of Physics, 104 Davey Laboratory, The Pennsylvania State University, University Park, PA 16802, USA
[5] INAF—Osservatorio di Astrofisica e Scienza dello Spazio di Bologna, Via Gobetti 93/3, 40129 Bologna, Italy

Received 2025 April 28; revised 2025 July 9; accepted 2025 July 29; published 2025 September 1

Abstract

Dust-obscured galaxies (DOGs) with extremely red optical-to-infrared colors are often associated with intense starburst and active galactic nucleus (AGN) activity. Studying DOGs can provide insights into the processes that drive the growth of galaxies and their central supermassive black holes. However, the general DOG population is heterogeneous, spanning a wide range of evolutionary stages, and has X-ray obscuring column densities ($N_{\rm H}$) covering low to high levels. In this work, we focus on seven high Eddington ratio DOGs ($\log \lambda_{\rm Edd} \gtrsim -0.5$) to examine their X-ray obscuration properties using new and archival X-ray observations. We confirm that these systems are generally heavily obscured, with six out of seven having $N_{\rm H} \gtrsim 10^{23}\,{\rm cm}^{-2}$ and three out of seven having $N_{\rm H} \gtrsim 10^{24}\,{\rm cm}^{-2}$. Based on the observed similarity with the rare Hot DOG population, we argue that both high-$\lambda_{\rm Edd}$ DOGs and Hot DOGs likely trace the postmerger phase, during which AGNs are enshrouded by large columns of dust-rich material.

Unified Astronomy Thesaurus concepts: Active galactic nuclei (16); Galaxy evolution (594); AGN host galaxies (2017)

1. Introduction

Within the coevolution framework of supermassive black holes (SMBHs) and their host galaxies (e.g., D. B. Sanders et al. 1988; P. F. Hopkins et al. 2006, 2008; D. M. Alexander & R. C. Hickox 2012), major mergers of gas-rich galaxies can trigger intense starburst activity and drive material toward the central SMBHs, fueling accretion. The peak activity of both SMBH accretion and star formation occurs during dust-enshrouded, heavily obscured phases, with the (obscured) SMBH accretion approaching the Eddington limit (e.g., D. Narayanan et al. 2010; E. Treister et al. 2010; G. B. Lansbury et al. 2015; F. Vito et al. 2018). Subsequently, radiation-driven outflows from near the central SMBH sweep away the obscuring material (in a "blow-out" phase; e.g., P. F. Hopkins & M. Elvis 2010; A. C. Fabian 2012 and references therein), allowing the SMBH to manifest as an unobscured active galactic nucleus (AGN).

Hot dust-obscured galaxies (Hot DOGs) and dust-obscured galaxies (DOGs) have been suggested to represent key postmerger evolutionary phases. Both are selected observationally for their extremely red optical and/or infrared (IR) colors (A. Dey et al. 2008; P. R. M. Eisenhardt et al. 2012; J. Wu et al. 2012, 2018; Y. Toba & T. Nagao 2016; Y. Toba et al. 2017), potentially representing the peak phase of SMBH accretion, AGN obscuration, and host star formation in the coevolution framework. Hot DOGs are detected by the Wide-field Infrared Survey Explorer (WISE) at 12 and 22 μm, but nearly undetected at 3.4 and 4.6 μm (P. R. M. Eisenhardt et al. 2012; J. Wu et al. 2012). They are a rare population with a sky surface density of approximately one candidate per 30 deg^2 and are thought to be primarily powered by deeply buried, massive SMBHs with high Eddington ratios ($\lambda_{\rm Edd}$). Their extreme optical/IR colors are thought to result from emission by hot dust, reaching temperatures up to 100s of K, heated by central SMBHs (e.g., C.-W. Tsai et al. 2015; J. Wu et al. 2018; G. Li et al. 2024).

DOGs are typically selected with 24 μm fluxes $f_{24\,\mu{\rm m}} \geqslant 0.3$ mJy and R-band to 24 μm colors $(R - [24])_{\rm Vega} \geqslant 14$ (A. Dey et al. 2008). Y. Toba & T. Nagao (2016) additionally applied a criterion of $f_{22\,\mu{\rm m}} \geqslant 3.8$ mJy and $i - [22] \geqslant 7$ to select IR-bright DOGs, which tend to have larger AGN contributions. DOGs are generally less extreme, characterized by less-massive SMBHs and larger host-galaxy contributions, and they have smaller intrinsic 2–10 keV luminosities ($L_{\rm X}$) compared to the rarer Hot DOGs. Compared to Hot DOGs, DOGs are more common and representative in the Universe. Numerically, the surface number density of DOGs on the sky can reach $\approx 300\,{\rm deg}^{-2}$ in deep fields (e.g., A. Dey et al. 2008; Z. Yu et al. 2024), but the surface number density of Hot DOGs is 4 orders of magnitude lower ($\approx 0.03\,{\rm deg}^{-2}$; P. R. M. Eisenhardt et al. 2012; J. Wu et al. 2012).

X-ray observations provide unique insights into the nature of (Hot) DOGs. One of the primary advantages of X-rays is their high penetration power, which enables the direct identification of AGNs buried in large column densities ($N_{\rm H}$) of obscuring material. Studies have found that Hot DOGs exhibit high $L_{\rm X}$ with nearly Compton-thick obscuration (D. Stern et al. 2014; R. J. Assef et al. 2016, 2020; C. Ricci et al. 2017a; F. Vito et al. 2018; L. Zappacosta et al. 2018). Notably, F. Vito et al. (2018) concluded that Hot DOGs occupy a distinct region in the $N_{\rm H}$–$L_{\rm X}$ plane, characterized by much higher $N_{\rm H}$ than luminous red type 1 quasars, which are thought to be transitioning from a heavily obscured phase to an unobscured blue-quasar phase.

However, the X-ray obscuration of DOGs spans a wider $N_{\rm H}$ range than that of Hot DOGs (G. Lanzuisi et al. 2009; A. Corral et al. 2016; L. A. Riguccini et al. 2019; N. Cristello et al. 2024; A. Kayal & V. Singh 2024; Z. Yu et al. 2024). This suggests that the DOG population may be heterogeneous, potentially covering a wide range of evolutionary stages, or even sometimes be explained by episodes of star formation, as concluded in Z. Yu et al. (2024) based on a large sample of well-characterized DOGs. Z. Yu et al. (2024) also demonstrated that the general DOG population is not primarily driven by major mergers and that typical AGN-containing DOGs are analogous to extreme type 2 AGNs instead of Hot DOGs. However, F. Zou et al. (2020) argued that high-$\lambda_{\rm Edd}$ DOGs naturally tend to be close to the dust-enshrouded phase after major mergers and, like Hot DOGs, are likely heavily obscured in X-rays. We note that previously identified DOG samples rarely reach $N_{\rm H} \gtrsim 10^{23.5}\,{\rm cm}^{-2}$, implying that heavily obscured DOGs (i.e., the analogs of Hot DOGs) may be severely underrepresented. The few reported heavily obscured DOGs (e.g., Y. Toba et al. 2020; F. Zou et al. 2020; N. Cristello et al. 2024) indeed also have high $\lambda_{\rm Edd}$.

To further constrain the X-ray obscuration levels of high-$\lambda_{\rm Edd}$ DOGs, we compile seven DOGs with known high $\lambda_{\rm Edd}$ values that are comparable to those of Hot DOGs (generally having $-0.5 \lesssim \log\lambda_{\rm Edd} \lesssim 0.5$; e.g., G. Li et al. 2024) and target four of them with Chandra observations in this work. The detailed sample selection will be presented in Section 2. We will probe if our sources are indeed heavily obscured, as has been seen for Hot DOGs, in Section 3. We adopt a flat ΛCDM cosmology with $H_0 = 70\,{\rm km\,s^{-1}\,Mpc^{-1}}$, $\Omega_\Lambda = 0.7$, and $\Omega_M = 0.3$. For simplicity, we will write SDSS Jhhmmss.ss ddmmss.s as Jhhmm ddmm in the main text. We will use $L_{\rm X}$ and $L_{\rm X,obs}$ to represent intrinsic and observed (i.e., without absorption corrections) 2–10 keV luminosities, respectively, unless otherwise noted. We will always adopt ${\rm cm}^{-2}$ as the unit of $N_{\rm H}$.

2. Sample Selection

Our sample is primarily drawn from the high-$\lambda_{\rm Edd}$ DOG sample in F. Zou et al. (2020), which initially came from Y. Toba & T. Nagao (2016) and Y. Toba et al. (2017). Y. Toba et al. (2017) systematically selected 36 IR-bright DOGs with $(i - [22])_{\rm AB} > 7$, 22 μm flux densities above 3.8 mJy, and clear [O III] from the Sloan Digital Sky Survey (SDSS). Among them, F. Zou et al. (2020) further selected sources with broad Mg II or H lines and targeted 12 DOGs with Cycle 20 Chandra snapshot observations (λ 3 ks per source). The goal of selecting broad-line DOGs is to measure their black hole masses ($M_{\rm BH}$) and, consequently, $\lambda_{\rm Edd}$, based on their broad-line widths, by assuming a virial equilibrium in the broad-line region. Measuring $M_{\rm BH}$ also requires intrinsic, deabsorbed AGN optical or UV luminosities (e.g., Y. Shen 2013). These were derived from spectral energy distribution (SED) fitting by recovering the deabsorbed AGN SED components, as has been done in F. Zou et al. (2020), and such techniques have also been implemented to measure $M_{\rm BH}$ values for Hot DOGs (e.g., G. Li et al. 2024). F. Zou et al. (2020) showed that these 12 DOGs generally have high $\lambda_{\rm Edd}$ and utilized Cycle 20 Chandra observations to examine their basic X-ray obscuration properties. All three targets with $\lambda_{\rm Edd} < 0.1$ were X-ray-detected, but only three out of nine sources with $\lambda_{\rm Edd} > 0.1$ were detected. At least at face value, the lower detection rates at higher $\lambda_{\rm Edd}$ may suggest that high-$\lambda_{\rm Edd}$ DOGs are more obscured. However, the short Chandra exposures in F. Zou et al. (2020) hindered more effective constraints on the X-ray absorption columns of high-$\lambda_{\rm Edd}$ DOGs.

To further improve the constraints on high-$\lambda_{\rm Edd}$ DOGs, we conducted follow-up X-ray observations with longer exposure. Given our available follow-up resources, we focus on the six DOGs with the higher half of $\lambda_{\rm Edd}$ in the sample of F. Zou et al. (2020) ($\log\lambda_{\rm Edd} \gtrsim -0.5$), as they are more representative of the extreme high-$\lambda_{\rm Edd}$ DOG population. As shown in G. Li et al. (2024), the $\lambda_{\rm Edd}$ of Hot DOGs is mainly distributed across $-0.5 \lesssim \log\lambda_{\rm Edd} \lesssim 0.5$ (see their Figures 6 and 7), and thus DOGs below $\log\lambda_{\rm Edd} \lesssim -0.5$ in F. Zou et al. (2020) are not formally high-$\lambda_{\rm Edd}$ DOGs with $\lambda_{\rm Edd}$ comparable to Hot DOGs. Besides, we do not have new observations of these lower-$\lambda_{\rm Edd}$ DOGs and thus do not have effective constraints on their $N_{\rm H}$. Therefore, the remaining DOGs with lower $\lambda_{\rm Edd}$ in F. Zou et al. (2020) will not be discussed in this work.

We have obtained a 68 ks follow-up XMM-Newton observation for the brightest X-ray source in the sample, J1324+4501, confirming its heavily obscured nature with $\log N_{\rm H} = 23.43^{+0.09}_{-0.13}$ (N. Cristello et al. 2024). In this work, we obtained longer Cycle 25 Chandra exposures (λ 15 ks per source) for the four fainter sources, where the exposures are set to ensure that even if these sources are undetected, the corresponding X-ray upper limits are sufficiently tight enough to confirm the heavily obscured nature. This work presents the new Chandra observations and combines these newly observed sources with the archival ones to provide constraints on the X-ray obscuration levels of high-$\lambda_{\rm Edd}$ DOGs.

Besides the six high-$\lambda_{\rm Edd}$ DOGs from F. Zou et al. (2020), we also supplement the sample with the single source, J0825+3002, reported in Y. Toba et al. (2020). This DOG was also derived from the initial IR-bright DOG sample in Y. Toba & T. Nagao (2016) and observed by XMM-Newton and NuSTAR, showing a Compton-thick $N_{\rm H} = 1.0^{+0.8}_{-0.4} \times 10^{24}\,{\rm cm}^{-2}$. Y. Toba et al. (2020) estimated its $M_{\rm BH}$ based on the scaling relation between $M_{\rm BH}$ and host-galaxy stellar mass, which places J0825+3002 to also be a high-$\lambda_{\rm Edd}$ DOG with $\lambda_{\rm Edd} = 0.7$. Although this $\lambda_{\rm Edd}$ measurement is indirect, we include this source for completeness. We note that explicitly reported high-$\lambda_{\rm Edd}$ DOGs are rare because it is generally challenging to confirm their high $\lambda_{\rm Edd}$. We include both samples from Y. Toba et al. (2020) and F. Zou et al. (2020) to represent the best knowledge we have regarding this population. Removing J0825+3002 out of our sample would not materially affect our overall conclusions in Section 4.

We summarize the properties of our sources in Table 1. The X-ray properties are either from the literature (the last three rows of the table) or will be derived in Section 3.2 (the first four rows of the table). For sources other than J0825+3002, the $M_{\rm BH}$ and $\lambda_{\rm Edd}$ are from Table 4 in F. Zou et al. (2020) and are all derived from broad Mg II lines. For J0825+3002, its $M_{\rm BH}$ is based on the scaled host stellar mass, as reported in Section 3.3 of Y. Toba et al. (2020).

Although the statistical $\lambda_{\rm Edd}$ uncertainties may not allow a firm conclusion on $\log\lambda_{\rm Edd} > -0.5$ for individual sources, they are sufficiently small to prove that our sample as a whole can represent high-$\lambda_{\rm Edd}$ DOGs. If adopting 0.5 dex as the nominal uncertainty for J0825+3002's $\log\lambda_{\rm Edd}$, the uncertainty of the weighted arithmetic mean $\log\lambda_{\rm Edd}$ of our sample would be only 0.06. However, systematic uncertainties are not directly considered here and may be more prominent. The

Table 1
Source Properties

SDSS Name (1)	z (2)	$\log M_{\rm BH}$ ($M_\odot$) (3)	$\log \lambda_{\rm Edd}$ (4)	$\log L_{\rm X,obs}$ (erg s^{-1}) (5)	$\log L_{\rm X}$ (erg s^{-1}) (6)	$\log N_{\rm H}$ (cm^{-2})
J104241.10+245107.0	1.026	8.80 0.15	−0.48 0.16	<42.8	$44.4^{+0.3}_{-0.4}$	>24.0
J121056.92+610551.5	0.926	7.89 0.33	−0.11 0.35	$42.5^{+0.3}_{-0.2}$	$43.6^{+0.8}_{-0.4}$	$23.3^{+1.6}_{-0.9}$
J123544.97+482715.4	1.023	8.20 0.12	−0.60 0.08	$43.4^{+0.1}_{-0.1}$	$43.8^{+0.1}_{-0.1}$	<22.5
J151354.48+145125.2	0.882	8.15 0.12	−0.33 0.16	<42.5	$44.1^{+0.3}_{-0.5}$	>23.9
J082501.48+300257.1[a]	0.890	8.40[b]	−0.15[b]	44.1	$44.6^{+0.2}_{-0.2}$	$24.0^{+0.3}_{-0.2}$
J132440.17+450133.8[a]	0.774	8.27 0.40	−0.06 0.40	$44.11^{+0.05}_{-0.04}$	$44.71^{+0.08}_{-0.12}$	$23.43^{+0.09}_{-0.13}$
J152504.74+123401.7[a]	0.851	8.36 0.23	−0.51 0.24	$43.3^{+0.2}_{-0.2}$	$44.3^{+0.3}_{-0.3}$	$23.2^{+0.3}_{-0.3}$

Notes. (2) Redshifts. All quoted redshifts are spectroscopic, except for J0825+3002, which only has a photometric redshift. (3) Black hole masses. (4) Eddington ratios. (5) 2–10 keV luminosities without absorption corrections. (6) Intrinsic (unabsorbed) 2–10 keV luminosities. For J1042+2451, J1210+6105, and J1513+1451, these measurements are primarily set by the prior instead of the X-ray data. (7) Intrinsic line-of-sight hydrogen-equivalent column densities. The confidence intervals of the measured values represent 68% levels, while the limits are at a 95% level.

[a] X-ray measurements for J0825+3002, J1324+4501, and J1525+1234 are from Y. Toba et al. (2020), N. Cristello et al. (2024), and F. Zou et al. (2020), respectively.

[b] The $M_{\rm BH}$ of J0825+3002 is estimated based on the scaling relation between $M_{\rm BH}$ and the host stellar mass. Therefore, its $M_{\rm BH}$ and $\lambda_{\rm Edd}$ have nominal uncertainties of λ 0.5 dex from the scaling relation.

most relevant uncertainty is the viability of using broad lines to infer $M_{\rm BH}$ for DOGs. In fact, the origin of the broad lines in such heavily X-ray obscured systems has been under continuous investigation. Relevantly, it is not uncommon for Hot DOGs to show broad lines (C.-W. Tsai et al. 2018; J. Wu et al. 2018; L. Finnerty et al. 2020; H. D. Jun et al. 2020; G. Li et al. 2024). The broad lines of some Hot DOGs are suggested to be potentially from outflows instead of the broad-line region (e.g., L. Finnerty et al. 2020; H. D. Jun et al. 2020). However, follow-up studies of a subpopulation of Hot DOGs that show significant excess blue emission (R. J. Assef et al. 2016, 2020, 2022) revealed that the blue emission and associated broad lines should be the scattered light from central AGNs based on, for example, multiwavelength and polarimetry observations. G. Li et al. (2024) further argued that for general Hot DOGs, their broad lines may also be mainly scattered emission, and hence these broad lines can be used to estimate $M_{\rm BH}$. For our DOGs specifically, F. Zou et al. (2020) showed that their broad Mg II line profiles are generally different from the outflow [O III] profiles (see their Section 5.2 for more discussion). Therefore, the broad lines of our sources are highly likely also from scattered emission from the broad-line regions. Nevertheless, an outflow origin cannot be deterministically ruled out, and this is a fundamental caveat for not only our DOGs but also all the Hot DOGs and relevant works in general.

3. Data and Results

In this section, we will first present the new Chandra observations (Section 3.1) and $N_{\rm H}$ constraints (Section 3.2) for four sources in our sample and then combine them with the remaining three archival sources in our sample to discuss the implications for high-$\lambda_{\rm Edd}$ DOGs (Section 3.3).

3.1. Chandra Data Reduction

The four sources with new Chandra Cycle 25 observations also have Cycle 20 observations; we summarize them all in Table 2. The data were reduced using `CIAO` 4.16 and `CALDB` 4.11.2. We first run the `chandra_repro` script with the option `check_vf_pha = yes`, since our observations were taken in Very Faint mode. We then use the `fluximage` script to generate images with weights according to a redshifted absorbed power-law model, where the redshift is set to the known value, the intrinsic $N_{\rm H}$ is set to 10^{24} cm^{-2}, and the photon index is set to $\Gamma = 2$. The weighting parameters are based on prior estimates indicating that our sources are highly obscured. Their exact values are not critical, and altering them does not affect the results. We further use the `specextract` script to extract X-ray spectra, grouped to at least one count per bin, and response files with 2 circular source regions and annulus background regions with inner and outer radii of 10 and 40 centered at the source position. As shown in Table 2, there is no apparent count-rate variability between the Cycle 20 and Cycle 25 observations, and we will jointly analyze them hereafter.

To assess whether the sources are detected, we calculate the binomial no-source probability P_B (P. S. Broos et al. 2007; M. C. Weisskopf et al. 2007). We set a detection threshold of $P_B = 0.01$, suitable for sources with known locations. By combining data from Cycle 20 and Cycle 25 observations, we successfully detected J1210+6105 (3 source-region counts) and J1235+4827 (17 source-region counts), with $P_B = 1 \times 10^{-3}$ and 2×10^{-26}, respectively; J1042+2451 and J1513+1451 are not detected.

We further constrain the expected net source counts within the source apertures using the method described in Appendix A of M. C. Weisskopf et al. (2007). The 68% confidence intervals for the counts of detected sources and the 95% upper limits for undetected sources are presented in Table 2.

3.2. N$_H$ Measurements

We convert the net counts to $L_{\rm X,obs}$ using a power-law model with $\Gamma = 1.4$ and the extracted Chandra response files. Figure 1 illustrates the comparison between $L_{\rm X,obs}$ and the AGN 6 μm luminosities, $L_{6\,\mu{\rm m}} = \nu L_\nu(6\,\mu{\rm m})$, for the entire sample. The $L_{6\,\mu{\rm m}}$ values were estimated by Y. Toba et al. (2020) and F. Zou et al. (2020) by decomposing the corresponding SEDs. The three archival sources (J0825+3002, J1324+4501, and J1525+1234) have reported

[illegible]

[illegible]	[illegible]	[illegible]	[illegible]	[illegible]	[illegible]
[illegible]	[illegible]	[illegible]	[illegible]	[illegible]	5
[illegible]	[illegible]	[illegible]	[illegible]	[illegible]	[illegible]
	[illegible]	[illegible]	[illegible]	[illegible]	
[illegible]	[illegible]	[illegible]	[illegible]	[illegible]	$2.8^{+2.9}_{-0.9}$
	[illegible]	[illegible]	[illegible]	[illegible]	
[illegible]	[illegible]	[illegible]	[illegible]	[illegible]	$16.8^{+5.2}_{-3.2}$
	[illegible]	[illegible]	[illegible]	[illegible]	
[illegible]	[illegible]	[illegible]	[illegible]	[illegible]	[illegible]
	[illegible]	[illegible]	[illegible]	[illegible]	

[illegible]

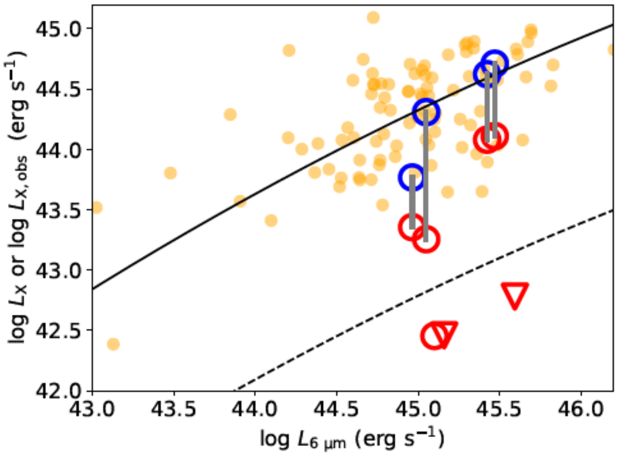

[illegible]

[illegible]

---

[5] [illegible]

colors are above the AGN mid-IR color selection criterion, W1 − W2 $\geqslant$ 0.8, in D. Stern et al. (2012), and are expected to be from AGN SEDs because AGNs are much redder than galaxies in the mid-IR. Figure 3 in F. Zou et al. (2020) also showed that strong AGN components are present in the mid-IR.

With the limited number of counts, we cannot simultaneously constrain $L_{\rm X}$ and $N_{\rm H}$ for the newly observed sources. Therefore, we focus on measuring $N_{\rm H}$ under the assumption that our sources follow the $L_{\rm X}$–$L_{6\,\mu{\rm m}}$ relation within a reasonable scatter. The spectral analyses are conducted with `Bayesian X-Ray Analysis` (`BXA`; J. Buchner et al. 2014) and `Sherpa` (A. Siemiginowska et al. 2024); the spectra are modeled with `phabs×(borus01+zphabs×cabs×cutoffpl)`, where `phabs` represents the Galactic absorption, `borus01` is the reprocessed spherical torus emission model of M. Baloković et al. (2018), `zphabs×cabs` models the source intrinsic absorption with Compton-scattering losses, and `cutoffpl` models the X-ray continuum. Since our sources may be in the dust-enshrouded phase, it is appropriate to adopt a covering factor of unity for the `borus01` model. Note that the `borus01` component only becomes important when $N_{\rm H} \gg 10^{24}\,{\rm cm}^{-2}$, and thus its detailed geometry has little impact on the qualitative inference of the heavy-obscuration nature of our sources. We fix the average $N_{\rm H}$ of the torus to $10^{24}\,{\rm cm}^{-2}$ and use the inferred $N_{\rm H}$ values of `zphabs` and `cabs` to represent the line-of-sight $N_{\rm H}$. We fix the `cutoffpl` power-law index and cut-off energy to $\Gamma = 2$ and 500 keV, respectively. The two free parameters of the model are thus $N_{\rm H}$ and $L_{\rm X}$. We adopt a flat prior for line-of-sight $\log N_{\rm H}$ within $20 \leqslant \log N_{\rm H} \leqslant 26$ and a normal prior for $\log L_{\rm X}$ centered at the $L_{6\,\mu{\rm m}}$-predicted values. The standard deviation (λ 0.5 dex) of the $\log L_{\rm X}$ prior accounts for the intrinsic scatter of the $L_{\rm X}$–$L_{6\,\mu{\rm m}}$ relation (0.4 dex) and the $L_{6\,\mu{\rm m}}$ uncertainties. Note that we are not placing the assumed $L_{\rm X}$ exactly on the $L_{\rm X}$–$L_{6\,\mu{\rm m}}$ relation; instead, the prior dispersion still allows $L_{\rm X}$ to deviate away by 1 dex within the 2σ range of the prior.

We deliberately adopted a physically motivated, weakly informative prior for $L_{\rm X}$ because, as mentioned earlier, we would like to measure how much the obscuration level needs to reach to explain the low $L_{\rm X,obs}$ if our sources follow the $L_{\rm X}$–$L_{6\,\mu{\rm m}}$ relation within a reasonable scatter. This is a both necessary and reasonable assumption. The necessity is based on the fact that our sources are limited in counts, and thus it is infeasible to simultaneously constrain $L_{\rm X}$ and $N_{\rm H}$ for at least J1042+2451, J1210+6105, and J1513+1451, which have less than three counts each. We can only constrain one of these two parameters (or their limits) after assuming the other one. Our adopted assumption is also reasonable. We have verified that both DOG samples in A. Corral et al. (2016) and Z. Yu et al. (2024) are in good consistency with our priors, as can be visually seen in Figure 1: Both samples have a dispersion of 0.38 dex around the expected $L_{\rm X}$–$L_{6\,\mu{\rm m}}$ relation in D. Stern (2015) and a much smaller median offset. Besides, as shown in Figure 1, the intrinsic $L_{\rm X}$ of four out of seven sources in our sample are in good consistency with the $L_{\rm X}$–$L_{6\,\mu{\rm m}}$ relation. As discussed earlier in this section, previous works also reported that both DOGs and Hot DOGs, either individually or as a sample, are not too far from the $L_{\rm X}$–$L_{6\,\mu{\rm m}}$ relation (e.g., C. Ricci et al. 2017a; F. Vito et al. 2018; L. Zappacosta et al. 2018; Y. Toba et al. 2020; N. Cristello et al. 2024; Z. Yu et al. 2024).

The sampling of the posterior probability distributions is conducted with `BXA`, which has internally implemented the nested sampling Monte Carlo algorithm in the `UltraNest` package, as presented in J. Buchner (2021). We integrate out $L_{\rm X}$ and show the sampled marginal line-of-sight $N_{\rm H}$ posterior distributions in Figure 2. The $N_{\rm H}$ posterior of J1235+4827 has an apparent peak at $\log N_{\rm H} \approx 23.3$. The posteriors of J1042+2451 and J1513+1451 are small at low $N_{\rm H}$ and reach plateaus at high $N_{\rm H}$, and thus we can constrain their $N_{\rm H}$ lower limits. In contrast, J1235+4827 has an $N_{\rm H}$ upper limit. The Appendix also shows that the posteriors are generally robust against reasonable changes of the prior. These $N_{\rm H}$ measurements are reported in Table 1 together with the other three high-$\lambda_{\rm Edd}$ DOGs (J0825+3002, J1324+4501, and J1525+1234) from Y. Toba et al. (2020), F. Zou et al. (2020), and N. Cristello et al. (2024). The X-ray spectra of these literature-reported DOGs generally have much higher constraining power, and thus their measurements will remain similar no matter if we apply the $\log L_{\rm X}$ prior to their data. Table 1 indicates that most of our sources are heavily obscured, potentially reaching a Compton-thick level.

Table 1 presents the inferred intrinsic $L_{\rm X}$. The measurements for J1042+2451, J1210+6105, and J1513+1451 are influenced by the prior, which is evident from the large uncertainties in $L_{\rm X}$. The intrinsic $L_{\rm X}$ values of the remaining sources better reflect the X-ray data constraints.

3.3. The N_H–$L_{\rm X}$ *and* N_H–λ_{Edd} *Planes*

We display all of our seven sources in the $N_{\rm H}$–$L_{\rm X}$ plane in Figure 3. For comparison, we also plot red type 1 quasars (T. Urrutia et al. 2005; S. Martocchia et al. 2017; G. Mountrichas et al. 2017; A. D. Goulding et al. 2018; G. B. Lansbury et al. 2020), Hot DOGs (D. Stern et al. 2014; R. J. Assef et al. 2016; C. Ricci et al. 2017a; F. Vito et al. 2018; L. Zappacosta et al. 2018), and DOGs (G. Lanzuisi et al. 2009; A. Corral et al. 2016; Z. Yu et al. 2024). Our sources have $L_{\rm X}$ values comparable to other DOGs, but they appear to be generally more obscured, with six out of seven of our samples having $N_{\rm H} \gtrsim 10^{23}\,{\rm cm}^{-2}$. Three of our sources—J0825+3002, J1042+2451, and J1513+1451—reside in the Compton-thick regime, a region that is largely unoccupied by other DOGs. Such a difference also exists between the higher-luminosity Hot DOGs versus red type 1 quasars, suggesting the possible physical link between high-$\lambda_{\rm Edd}$ DOGs and Hot DOGs.

Furthermore, the $N_{\rm H}$–$\lambda_{\rm Edd}$ plane also serves as a useful diagram relevant to AGN-driven outflows (e.g., W. Ishibashi et al. 2018). Recall that the classical Eddington limit is defined for pure ionized hydrogen and only includes the electron scattering cross section. Real astronomical systems, however, usually have dusty gas instead, and dusts have a much higher overall absorption cross section compared to gas. A. C. Fabian et al. (2006) introduced the phrase "*effective* Eddington limit" to account for the dust absorption cross section, where AGNs with effective Eddington limits above the unity are expected to generate outflows. As detailed in W. Ishibashi et al. (2018), the effective Eddington limit can be expressed as a function of $\lambda_{\rm Edd}$ and $N_{\rm H}$, and the curve of an effective Eddington limit of unity divides the $N_{\rm H}$–$\lambda_{\rm Edd}$ plane into a "forbidden region" (also known as the outflow region) and an "allowed region" (e.g., D. Kakkad et al. 2016; C. Ricci et al. 2017b; W. Ishibashi

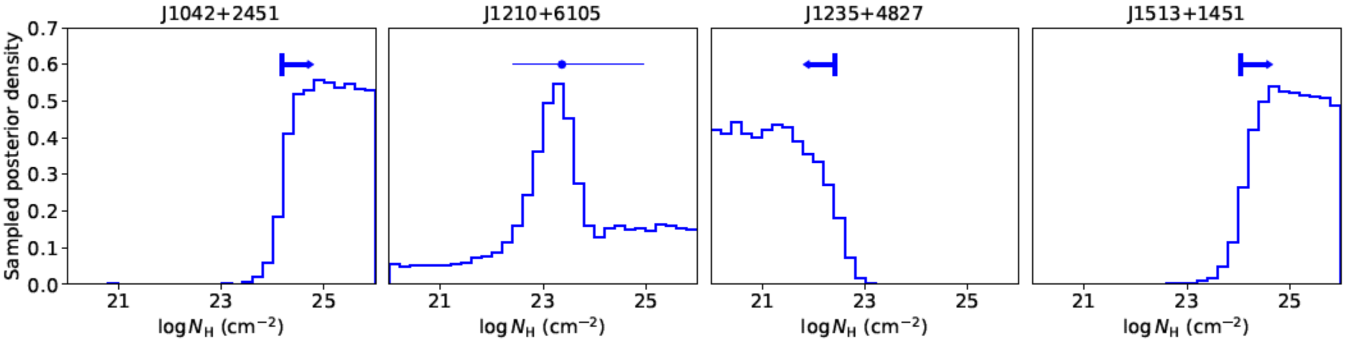
J1042+2451
J1210+6105
J1235+4827
J1513+1451
Sampled posterior density
0.0
0.1
0.2
0.3
0.4
0.5
0.6
0.7
21
23
25
log N_H (cm^{-2})

[illegible]

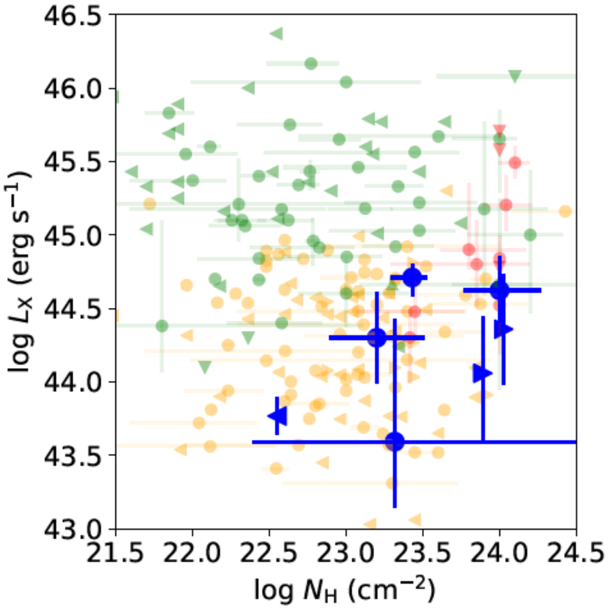
log L_X (erg s^{-1})
log N_H (cm^{-2})
43.0
43.5
44.0
44.5
45.0
45.5
46.0
46.5
21.5
22.0
22.5
23.0
23.5
24.0
24.5

[illegible]

[illegible]

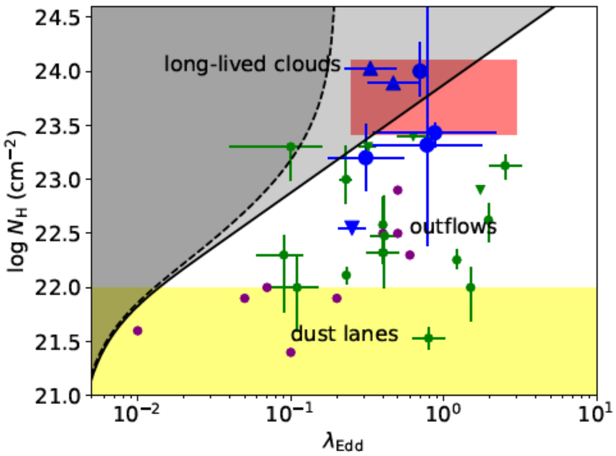
long-lived clouds
outflows
dust lanes
log N_H (cm^{-2})
$\lambda_{\rm Edd}$
21.0
21.5
22.0
22.5
23.0
23.5
24.0
24.5
10^{-2}
10^{-1}
10^{0}
10^{1}

[illegible]

[illegible]

[illegible]

[illegible]

[illegible]

[illegible] $\log \lambda_{\rm Edd} \gtrsim -0.5$ [illegible] $\log L_{\rm X}$ [illegible] $\gtrsim$ [illegible] $\gtrsim$ [illegible]

[illegible]

[illegible]

[illegible]

[illegible]

[illegible]

[illegible]

[illegible]

[illegible] $\log L_{\rm X}$ [illegible]

[illegible] $\log L_{\rm X}$ [illegible] $\log N_{\rm H}$ [illegible] $\log N_{\rm H}$ [illegible]

[illegible] $\log L_{\rm X}$ [illegible] $\log L_{\rm X}$ [illegible] $\log N_{\rm H}$ [illegible] $\log L_{\rm X}$ [illegible]

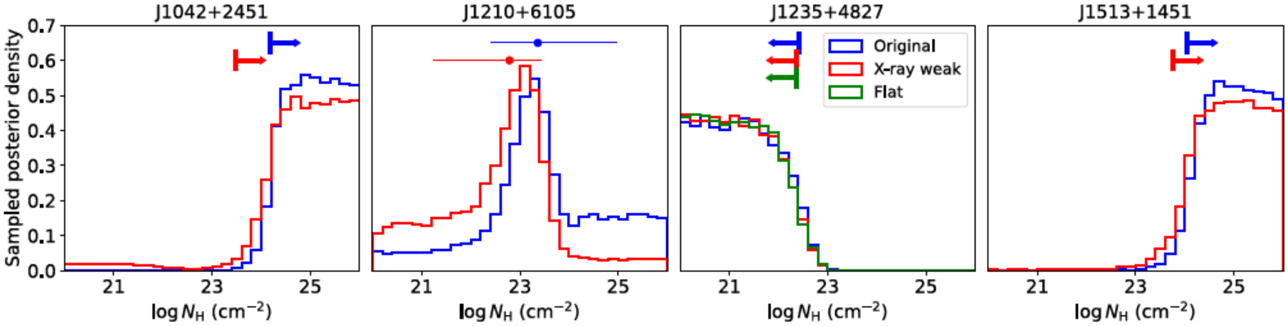

[illegible] log $N_{\rm H}$ [illegible] log L_X [illegible] log L_X [illegible] log L_X [illegible]

[illegible]

[illegible]

[illegible]

[illegible]